

Semester Thesis

**Solitons and Frequency
Combs in Quantum Cascade
Lasers****Autumn Term 2023**

Declaration of Originality

I hereby declare that the written work I have submitted entitled

Solitons and Frequency Combs in Quantum Cascade Lasers

is original work which I alone have authored and which is written in my words.¹

Author

Marcel Köberlin

Supervisor

Paolo Micheletti

Supervising Professor

Giacomo Scalari

With the signature, I declare that I have been informed regarding normal academic citation rules and that I have read and understood the information on 'Citation etiquette' (<https://www.ethz.ch/content/dam/ethz/main/education/rechtliches-abschluesse/leistungskontrollen/plagiarism-citationetiquette.pdf>). The citation conventions usual to the discipline in question here have been respected.

The above-written work may be tested electronically for plagiarism.

Place and date

Signature

¹Co-authored work: The signatures of all authors are required. Each signature attests to the originality of the entire written work in its final form.

Contents

1 Theory	5
1.1 Quantum Cascade Laser	5
1.2 Dissipative Kerr Solitons	5
1.3 Frequency Combs	6
1.4 Devices	7
1.4.1 Ring QCL	7
1.4.2 Single mode injected double ridge QCL	9
1.5 Regenerative THz detectors	9
1.6 SWIFTS: Shifted Wave Interference Fourier Transform Spectroscopy	10
2 Setup	11
2.1 Mounting	11
2.2 Main Setup	11
2.3 Device characterization	11
3 Results and Analysis	13
3.1 Ring QCL	13
3.2 Double Ridge QCL	19
4 Discussion	26

1 Theory

A short theoretical introduction to the topic is given.

1.1 Quantum Cascade Laser

In the simplest model, conventional solid-state lasers operate on laser transitions between the electronic bands between a semiconductor's conduction and valence bands. In contrast, the Quantum Cascade Laser (QCL) achieves lasing by using transitions between subbands in a semiconductor [1][2]. To get a subband structure, one typically uses layers of different semiconductor materials to build a superlattice. The cascading comes from the applied electric field, which causes a Stark effect throughout the structure. Throughout the QCL, there are multiple periods of active and injection regions. Population inversion is established in the prior, while the latter cools the electron distribution.[2] The working principle is schematically shown in figure (1). Note that the cascading, in principle, allows for quantum efficiencies greater than one, as one tunnelling electron will emit multiple photons, one in each period of the active region.

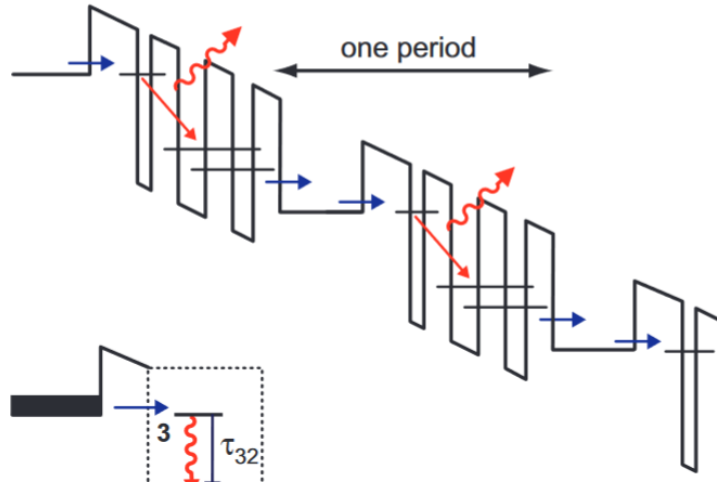


Figure 1: A schematic diagram depicting the QCL and one period of active and injection region [2].

QCLs can emit broadly, from the mid-infrared to the THz spectrum. The latter is especially relevant as obtaining sources in that frequency range, often referred to as the "THz gap", is particularly difficult. While room temperature operation has already been achieved in mid-infrared QCLs, it is much harder to accomplish in the THz region. One big problem is the low photon energy compared to the optical phonon energy, favouring phenomena such as thermal backfilling, which destroys population inversion. Therefore, operation at cryogenic temperatures is required to achieve population inversion [2].

1.2 Dissipative Kerr Solitons

The Kerr effect causes the refractive index of a nonlinear material to be intensity-dependent, e.g. $n(I) = n + n_2 I$, implying a nonlinear phase shift of $\varphi(t) = -kn(I)L = -knL - \delta I(t)$, where $\delta = kn_2 L$ is the self-phase modulation (SPM)

coefficient [3]. The presence of the Kerr effect implies a spectral broadening of the pulse, as the instantaneous frequency is now generally time-dependent, e.g.

$$\omega(t) = \frac{d\varphi}{dt} = -\delta \frac{dI}{dt}.$$

In the leading edge of the pulse, where $dI/dt > 0$, the instantaneous frequency is negative such that lower frequencies are generated, and the opposite is true in the trailing edge of the pulse.

In most materials, the non-linear refractive index n_2 is positive and of the order of $n_2 \sim 10^{14} \frac{\text{cm}^2}{\text{W}}$ [3]. If negative GVD is present, the effect can cancel with SPM, such that a stable wave-packet forms, the soliton $A(t) = A_0 \operatorname{sech}(t/\tau) e^{i\phi_0(z)}$.

It is self-reinforcing, as it will automatically find the correct shape, implying that small perturbations have little effect on the pulse shape, assuming they can be treated as continuous. This allows the solitonic pulse to propagate without changing its shape. It is worth noting that the soliton is the fundamental solution to the nonlinear Schrödinger equation [3].

QCLs are promising candidates to produce Kerr solitons, as they offer very large Kerr nonlinearities of the intersubband transitions [4]. Therefore, to counter this effect, we require a negative group velocity dispersion (GVD), which requires dispersion-compensated waveguides. Further, the pump and resonator are automatically integrated on the same chip, allowing for small devices. As we will see later, ring QCLs are a promising architecture, as they avoid SHB, thus producing solitons instead of frequency-modulated combs. However, these rings need to be defect-less to avoid backscattering, which would lead to SHB. Low scattering, in turn, implies poor power performance.

1.3 Frequency Combs

The output of a modelocked laser ideally consists of equally spaced pulses in time, e.g. a delta comb. This corresponds to a delta comb in frequency, such that every frequency in the spectrum can be described by [2][3]

$$f_n = f_{\text{CEO}} + n f_{\text{rep}}.$$

where f_{CEO} stands for carrier-envelope offset and f_{rep} stands for the repetition frequency, e.g. the distance between the spectral lines. A special case is soliton modelocking, where the resulting pulse envelope has solitonic shape, propagating the waveguide without changing its shape. Figure (2) schematically shows a frequency comb.

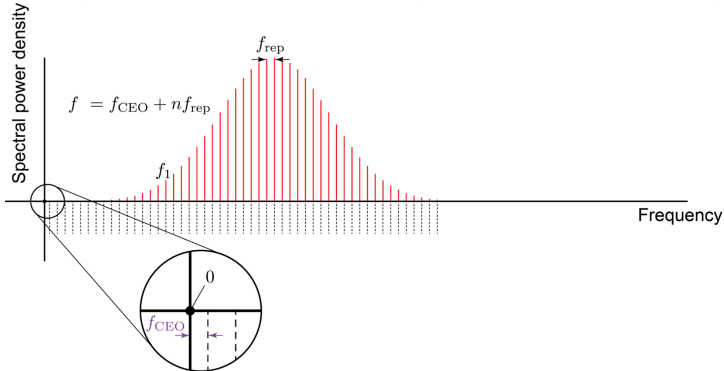


Figure 2: A frequency comb with repetition frequency f_{rep} and carrier-envelope offset f_{CEO} [3].

Frequency combs have many applications, such as fundamental time metrology, spectroscopy and frequency synthesis. They act as spectral rulers, allowing a direct link between radio frequency and optical frequencies [3]. A ring QCL produces a frequency comb with a repetition frequency

$$f_{\text{rep}} = \frac{c}{2\pi n_{\text{eff}} R},$$

such that one wants a large radius R to get a dense comb, e.g. low repetition frequency. However, a large radius implies high operating currents that prevent CW operation for thermal reasons. This can be avoided by narrowing the waveguide and suppressing higher-order modes.

The process to achieve frequency combs is a nonlinear process called four-wave mixing, requiring high third-order nonlinearity $\chi^{(3)}$ [5].

1.4 Devices

It is widespread to adopt double metal waveguides, confining radiation in a region of around $10\mu\text{m}$. Note that the THz region corresponds to wavelengths bigger than $100\mu\text{m}$, e.g. the waveguide size is sub-wavelength [2]. Another often adapted solution is to planarize the device using BCB planarization [6]. The advantage of using benzocyclobutene (BCB) planarization is that the bonding wires do not directly sit on the ridge, allowing for narrow waveguides, as well as decoupling the active region design from the top contact [2]. The process is shown figure (3).

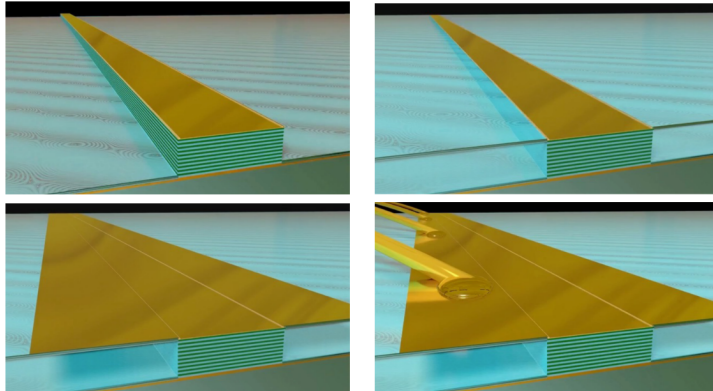


Figure 3: The process of using BCB to planarize the design [2].

BCB is a polymer with very low losses in the THz range and can be deposited on the chip by spinning. In the course of this project, multiple different active region designs were tested and classified. In the following, I will focus on the ring QCL and the double-ridge laser.

1.4.1 Ring QCL

As the name suggests, the active region in a ring QCL is ring-shaped. Rings are a promising design architecture, as they avoid spatial hole burning that can occur in standard ridge lasers caused by standing waves and fast saturable gain [7]. Figure (4) shows the two coupled ring-shaped waveguides.

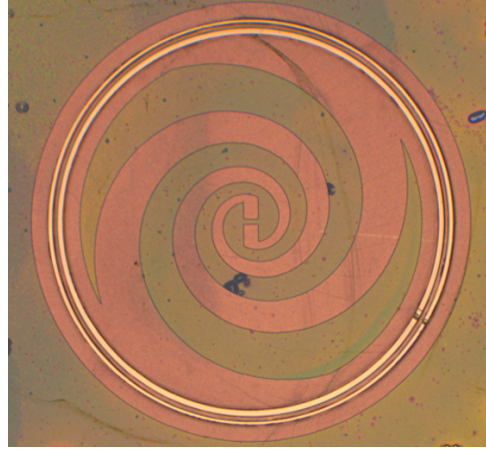


Figure 4: Image of a ring QCL with antenna.

If the physical spacing between the two waveguides is small enough, symmetric and antisymmetric supermodes form in the ring, with enhanced or suppressed GVD, respectively. However, the antisymmetric mode has a more significant overlap factor Γ , automatically causing the laser to select this mode with negative GVD. Figure (5) shows the effective refractive index n_{eff} , the simulated GVD and the overlap factor Γ for both supermodes.

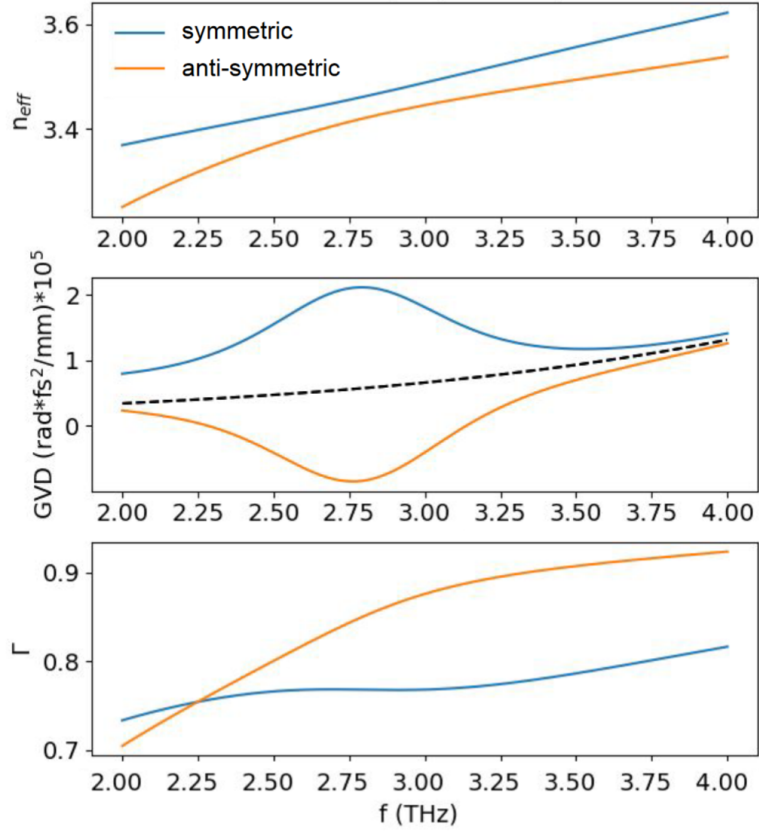


Figure 5: The effective refractive index, the group velocity dispersion and the overlap factor as a function of frequency.

A ring QCL emits light in all directions. To improve the far-field behaviour, antennas and output couplers such as a bullseye antenna can be used. To broaden the region with negative GVD, a chirped gap between the active region rings can be used, as figure (6) shows.

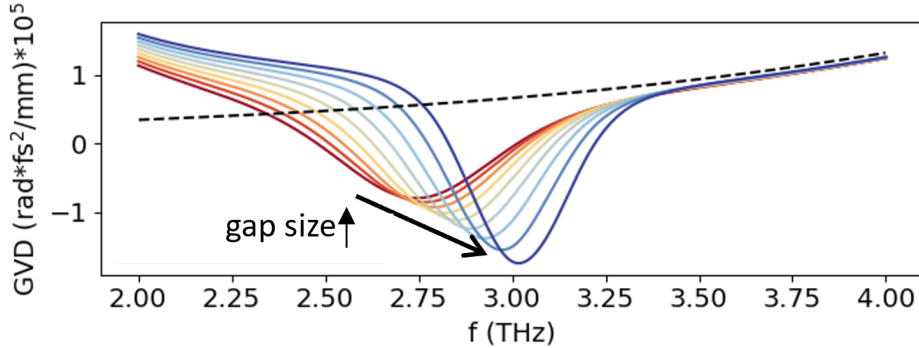


Figure 6: The effect of chirping the gap on the GVD.

1.4.2 Single mode injected double ridge QCL

The second promising device is a SM injected double ridge QCL featuring a low reflectivity facet, as figure (7) shows.

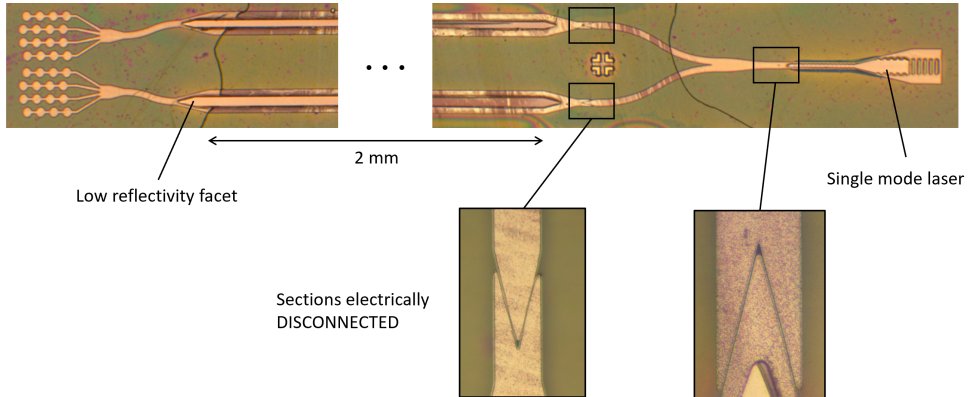


Figure 7: Image of a double ridge laser with low reflectivity facet.

The idea behind this structure is that we get two combs that are locked together by a single-mode laser, which can inject one mode into both. This allows fixing the repetition frequency with the injected RF, and the carrier-envelope offset frequency can be fixed by single-mode injection. If two combs with each other, it results in another comb at RF frequency, effectively down-converting to frequencies that are accessible by a standard spectrum analyzer. The active region is about 2mm long and connects to a single-mode laser. The highlighted sections are electrically disconnected.

1.5 Regenerative THz detectors

Classifying and measuring a THz source requires a suitable detector with high responsivity and low noise. Further, it needs to be fast enough to keep up with the ultrafast and photon-driven nature of the active region of the QCL, and operation

at room temperature is desired [8]. The idea is to use another THz QCL with high slope efficiency $\frac{dP}{dT}$ just below the lasing threshold. Due to the addition of photon-driven transport at the threshold, the IV curve will show a conductance discontinuity at the lasing threshold.

1.6 SWIFTs: Shifted Wave Interference Fourier Transform Spectroscopy

To characterize the phases of the modes, we combine a traditional FTIR with an ultrafast superconducting Hot-Electron Bolometer. It is a technique to measure temporal profiles in periodic signals by observing the beat note as a function of the delay of an FTIR. Figure (8) shows the measurement setup of SWIFTs.

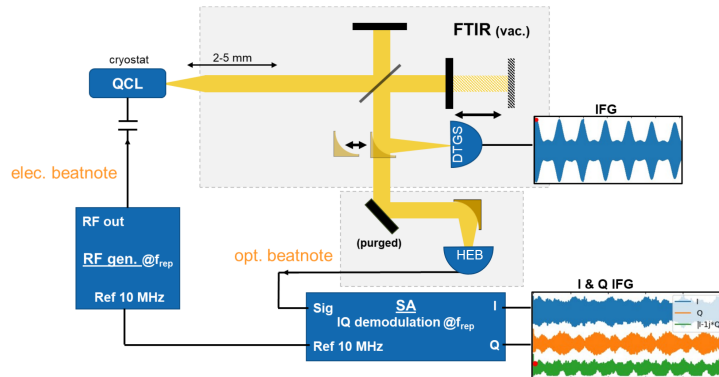


Figure 8: Setup of a general SWIFT spectroscopy measurement.

The following discussion closely follows [9]. The instantaneous power at the output of a Michelson interferometer is proportional to

$$S(t, \tau) = \frac{1}{2}(E(t) + E(t-\tau))^2 = \frac{1}{2} \sum_{n,m} E_n E_m^* e^{i(\omega_n - \omega_m)t} (1 + e^{-i(\omega_n - \omega_m)\tau} + 2e^{i\omega_m\tau}),$$

where $E_n = E(w_n)$ is the Fourier transform of $E(t) = \sum_n E_n e^{i\omega_n t}$. In conventional Fourier-transformed spectroscopy, the detector records the signal $S_0(\tau) = \langle S(t, \tau) \rangle$, with the integration being performed over lab timescales of Hz.

In SWIFTs, the power is demodulated with an arbitrary local oscillator at frequency ω_0 , such that the recorded signal is

$$\begin{aligned} S_+(\tau) &= \langle S(t, \tau) e^{-i\omega_0 t} \rangle = \sum_n \langle E(\omega_n + \omega_0) E^*(\omega_n) \rangle \left(\frac{1}{2} + \frac{1}{2} e^{-i\omega_0\tau} + e^{i\omega_n\tau} \right) \\ &= \sum_n \langle E_{n+1} E_n^* \rangle \left(\frac{1}{2} + \frac{1}{2} e^{-i\omega_0\tau} + e^{i\omega_n\tau} \right). \end{aligned}$$

For the last step, we assumed that the source structure is a frequency comb with matching repetition and local oscillator frequencies. There are three terms: two non-interferometric DC terms and one interferometric term. In the next step, we divide the recorded signal in terms of its quadratures S_I and S_Q :

$$S_+(\tau) = S_I(\tau) + iS_Q(\tau).$$

Finally, the phase of each SWIFTs line can be interpreted as a group delay, and the quadratures are measurable quantities, as they are real-valued.

2 Setup

A concise overview of the setup is provided; nevertheless, it is essential to acknowledge that this section will be brief, as the primary emphasis is directed towards the results presented in Chapter (3). The acquisition process of a QCL is both lengthy and Complex. Consequently, limited attention is dedicated to this aspect. The devices to be tested emerged from the cleanroom in a pre-assembled state, and my involvement was primarily confined to the final stage—mounting.

2.1 Mounting

First, one substrate usually contains multiple devices on it, as that saves time and resources. To divide them individually, cleaving needs to be done. After cleaving, the lasers are disconnected from each other, and the next step is to die bond them onto a copper plate, with indium in between. Copper offers excellent thermal and electrical conductivity and is, therefore, a good choice. Using silver paste, the grounding is established. The next step is to fix a PCB to the laser, which is done by using screws. Finally, wire bonding connects the PCB waveguide and the top contact.

2.2 Main Setup

Working with THz QCLs, cooling is an integral part of the experiments. The device is mounted on a cryostat to cool down to a known temperature. The environment and its thermal energy greatly impact the measurement's outcome: The upper state's lifetime goes as $\tau_3 \propto \frac{1}{T}$ so that a high temperature decreases the upper state lifetime [2]. This, in turn, makes achieving population inversion harder and decreases the gain. Thus, liquid helium was used to cool. Liquid helium is easy to control and allows for temperatures down to 4K [10]. It is stored in a dewar that connects to the device via transfer line. Since the boiling temperature of LH is very low, it will slowly expand over time and increase the pressure in the tank. Therefore, checking the pressure and keeping the display below 0.3 bar is essential. A safety valve will release excess LH to lower the pressure in case of high pressure. To not waste the released excess, a recovery line is connected to keep waste and losses at a minimum, as LH is not cheap after all.

Low temperature alone does not suffice; low pressure inside the laser chamber is required. This is done by letting a pre-vacuum pump run, followed by an ultra-vacuum pump. The pressure at the end is of the order of 10^{-7}bar .

2.3 Device characterization

There are many possible measurements; in this section, I want to highlight some techniques most often used in this project.

IV and LIV After the device is connected to cooling and control electronics, usually, the first experiment serves the purpose of characterizing and classifying the laser. To do so, the laser is driven in pulsed mode with a low duty cycle at usually not too low temperatures (20 – 40K), while an oscilloscope measures bias voltage V and current flowing through the device I . The lasing threshold and the negative differential resistance region can be found in this way. The threshold is characterized by a bump in the IV curve, namely a significant change in the slope of the curve. At this point, the gain in the active medium equals the losses, and the increase in photon population inside the cavity above the threshold makes the transport highly efficient. The NDR can be identified when the current decreases as

the bias voltage increases. The injector and upper electronic states are misaligned at a high enough applied bias voltage. Knowing the NDR is essential to know the maximal operating point of the QCL. Figure (9) shows an exemplaric IV curve.

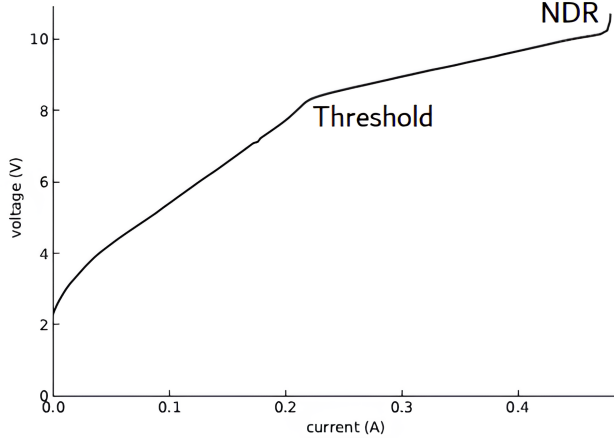


Figure 9: Exemplaric IV curve for a laser. The laser starts to lase at the threshold, where the slope abruptly changes.

To measure an LIV curve, one has to further measure the output power with a detector placed directly in front of the laser. A sudden nonzero output power can determine the lasing threshold as the laser emits coherent light. Above the threshold, the output power increases linearly with the current.

Fourier-transform infrared spectroscopy FTIR spectroscopy covers the entire operational range of THz QCLs. Further, it offers great sensitivity, allowing the detection of weak signals and high resolution. High resolution is important to identify different lasing modes precisely.

Spectrum It is crucial to know the spectrum of a laser, as it provides information about the different lasing modes. It further provides insight into the coherence of our device; a narrow linewidth indicates significant coherence. We drive the QCL in pulsed or CW mode to get the spectrum, always ensuring a stable temperature. If the output exhibits single-mode lasing, injecting an RF signal at the repetition frequency f_{rep} into the QCL can induce multimode operation, favouring the nonlinear process responsible for mode proliferation. This effect strongly depends on the delivered RF power; if the power of the injection is too low, no comb formation can be observed, whereas a high injection power turns the QCL unstable and thus destroys its coherence. This implies that a good spot exists to choose the power of the RF signal.

The sweet spot does not just exist in power but also in frequency. The optimal frequency might differ from the theoretical repetition frequency due to imperfections. Thus, a sweep is first performed in frequency, and when a suitable spot has been identified, a sweep in power is performed. Since this process is time-consuming, one usually does a coarse sweep, followed by a finer sweep in a smaller region. A symmetric interferogram is a first sign of coherence.

3 Results and Analysis

The results of the different designs are highlighted below.

3.1 Ring QCL

As always, the first experiment is an IV to find the threshold and NDR. This was done at 20K in pulsed mode. One can see in figure (10) that the threshold is at 300mA or $150 \frac{\text{A}}{\text{cm}^2}$. The area of the ring QCL was 0.2mm^2 .

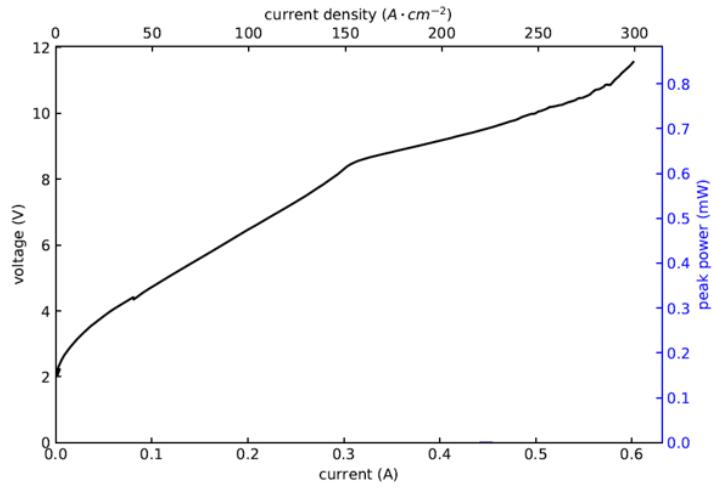


Figure 10: The IV curve of the ring QCL. The threshold is 300mA or $150 \frac{\text{A}}{\text{cm}^2}$.

Next, we look at the spectrum from 380mA to 500mA and see that the laser operates in single mode at 30K. This is shown in figure (11).

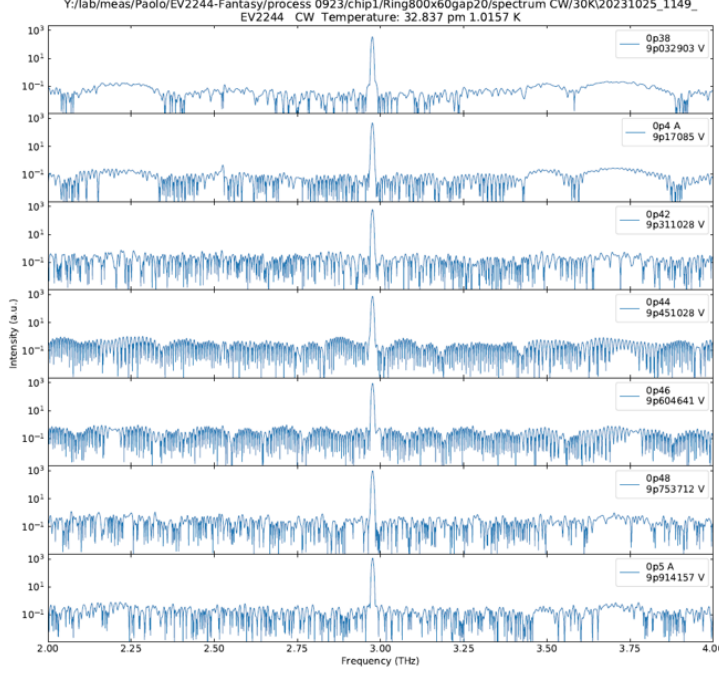


Figure 11: The spectrum of the ring QCL from 380mA to 500mA.

After identifying the spectrum, threshold, and NDR, the first task is to find the sweet spot in power. This is done by a power sweep from -5dBm to 35dBm . The laser was operated at 540mA, and the RF frequency was set to 15.65GHz. Figure (12) shows a colour plot, where colour represents the spectral intensity in a log scale.

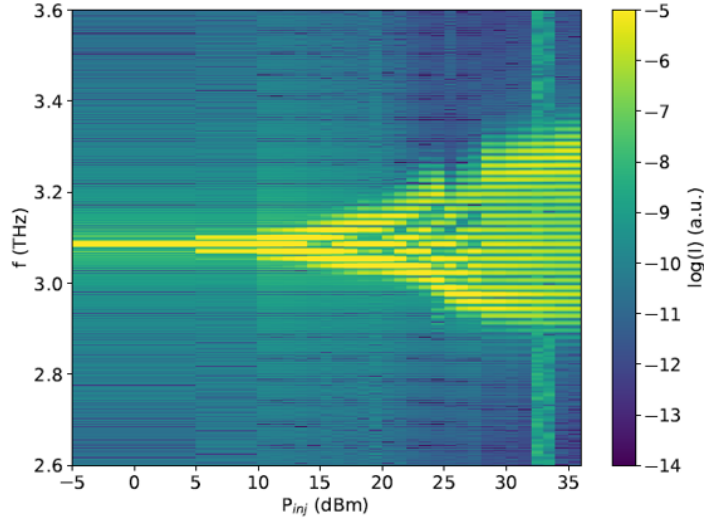


Figure 12: A colour plot of the laser spectrum vs the RF injection power.

As we can see, the laser starts in single mode since the RF signal power is initially too weak to modify the spectrum. As the power slowly increases, more lasing modes show up, and the spectrum becomes broader. 25dBm was identified to be

an excellent spot to continue the search for the optimal RF frequency. Figure (13) shows the spectrum for 25dBm.

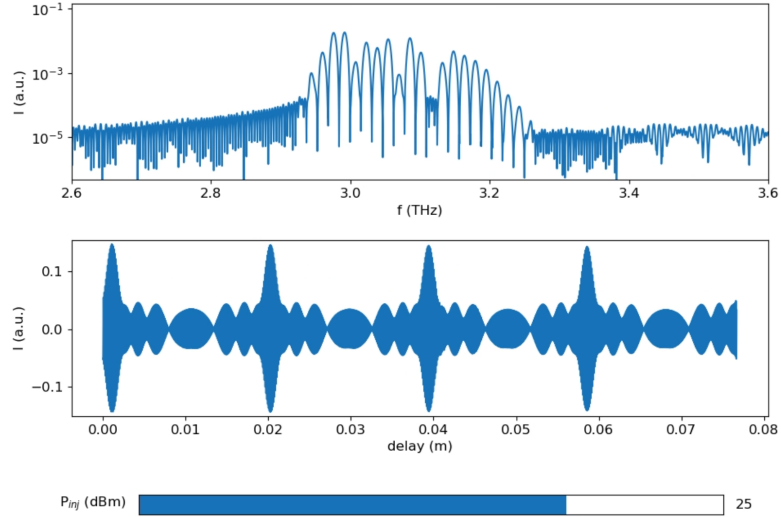


Figure 13: The laser spectrum at 25dB injected power shows a symmetric interferogram and a wide spectrum.

To find a good spot in RF frequency, a frequency sweep from 15.15GHz to 16.1GHz is performed. The result is shown in figure (2).

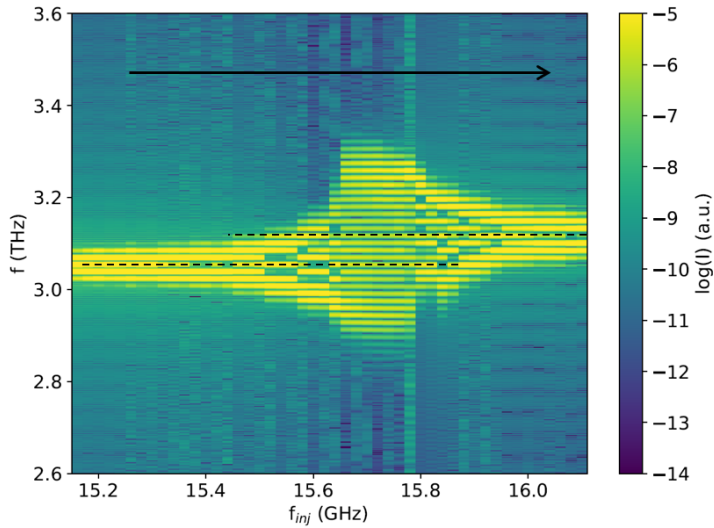


Figure 14: A frequency sweep from 15.15GHz to 16.1GHz shows hysteretic behaviour and needs to be studied more.

It is interesting to observe that the QCL exhibits hysteretic behaviour. The centre frequency of the spectrum is initially around 3.05THz. Increasing the injection frequency broadens the spectrum, reaching a maximal bandwidth of ≈ 450 GHz at 15.7GHz. Increasing the injection frequency further, the spectrum ends up in a low bandwidth state, centred around 3.12THz. We see a shift in the centre frequency of the spectrum. Figure (15) shows a spectrum at an RF frequency of 15.7GHz.

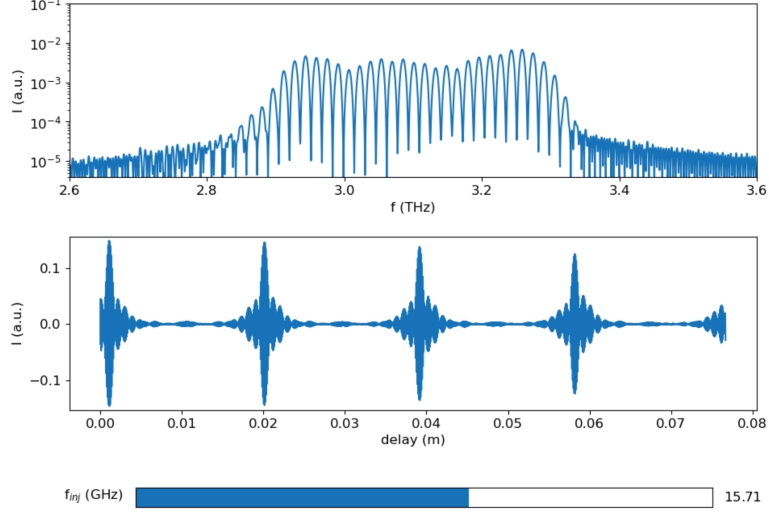


Figure 15: The laser spectrum and interferogram at 15.71GHz RF injection frequency.

To analyze this behaviour further, we do the same thing backwards, e.g., we start to sweep with high RF frequency and gradually lower it. This is shown in figure(16).

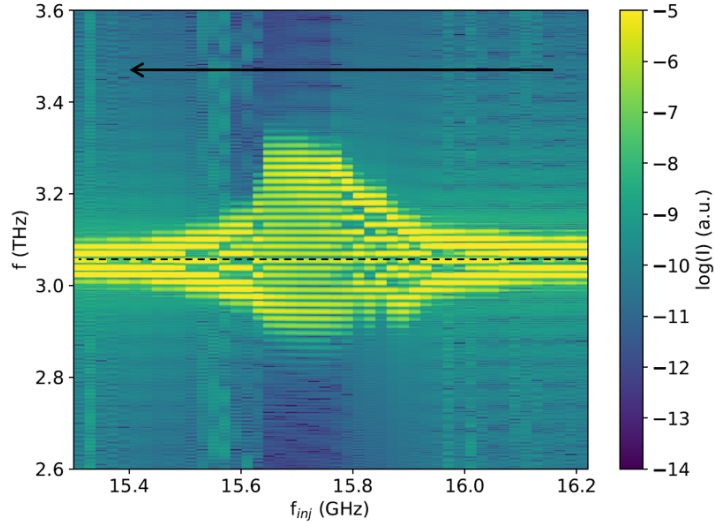


Figure 16: A frequency sweep backwards, starting from high injection frequency and gradually lowering it.

The system does not exhibit hysteretic behaviour. The centre frequency of the spectrum did not shift. However, a broadening of the spectrum is still observed for RF frequencies from 15.6GHz to 15.8GHz.

The following figures (17),(18),(19) and (20) show the spectrum, the phase, and I and Q values, as well as the time-resolved spectrum at frequencies 15.3GHz, 15.6GHz, 15.7GHz and 15.8GHz, respectively.

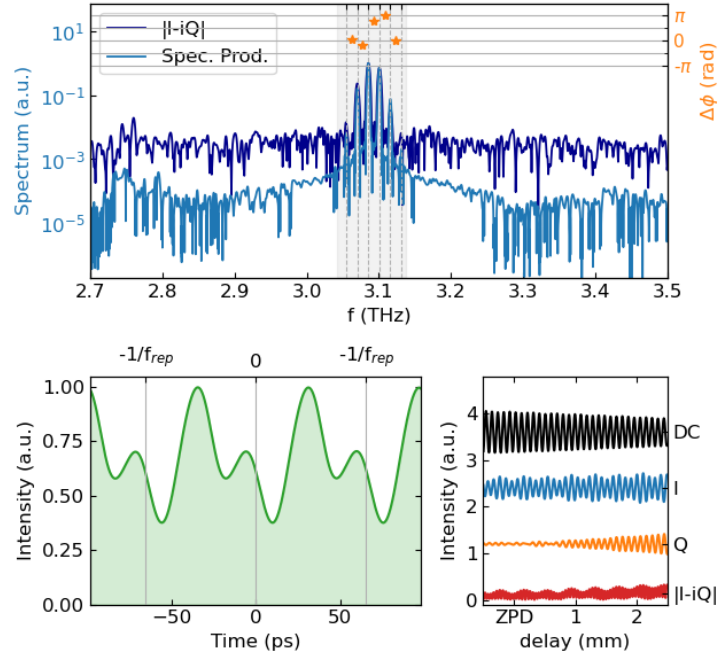


Figure 17: The spectrum, phase, the I and Q values, and the time-resolved spectrum at 15.3GHz.

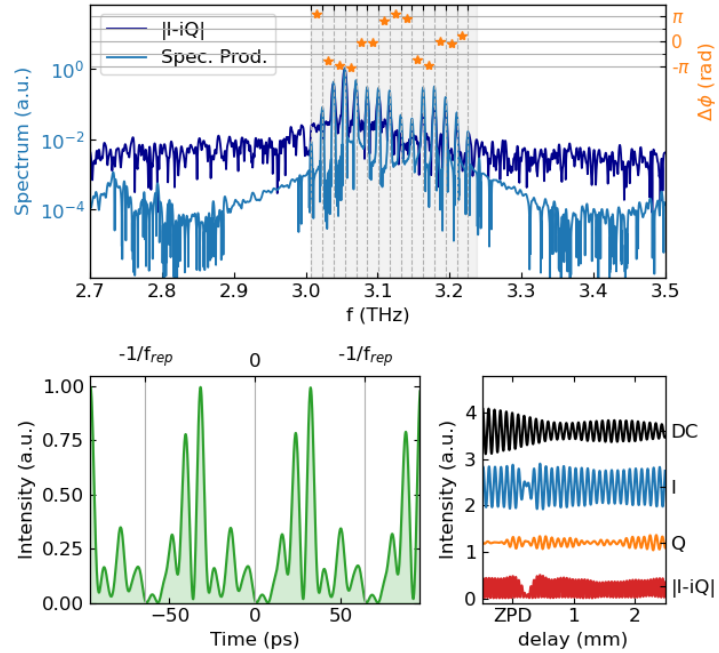


Figure 18: The spectrum, phase, the I and Q values, and the time-resolved spectrum at 15.6GHz.

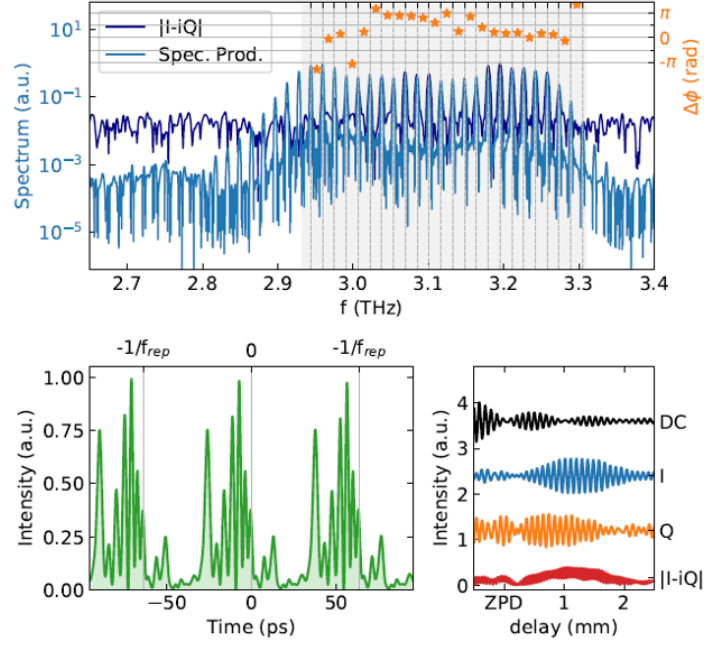


Figure 19: The spectrum, phase, the I and Q values, and the time-resolved spectrum at 15.7GHz.

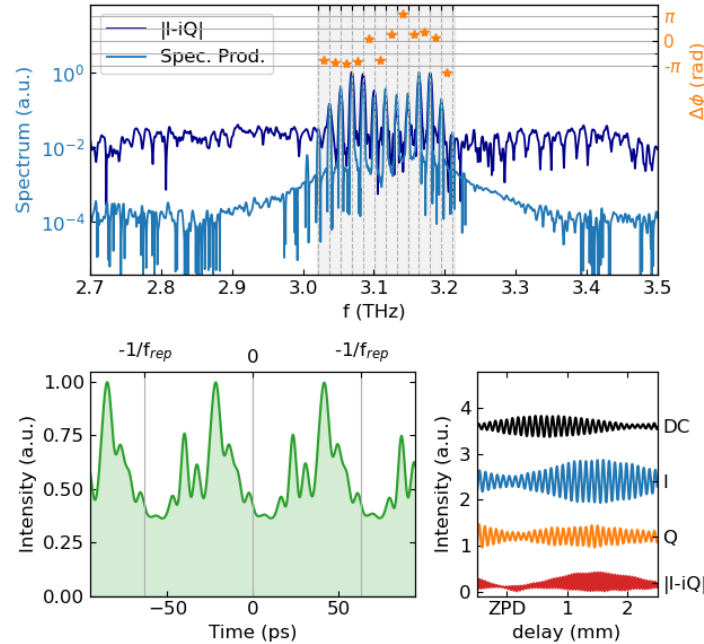


Figure 20: The spectrum, phase, the I and Q values, and the time-resolved spectrum at 15.8GHz.

3.2 Double Ridge QCL

As before, we started by taking IVs of the device. Since we now have a double ridge QCL, e.g., two coupled QCLs, we classify each QCL separately, e.g., drive only one at a time. Figure (21) shows the LIV for "laser 1".

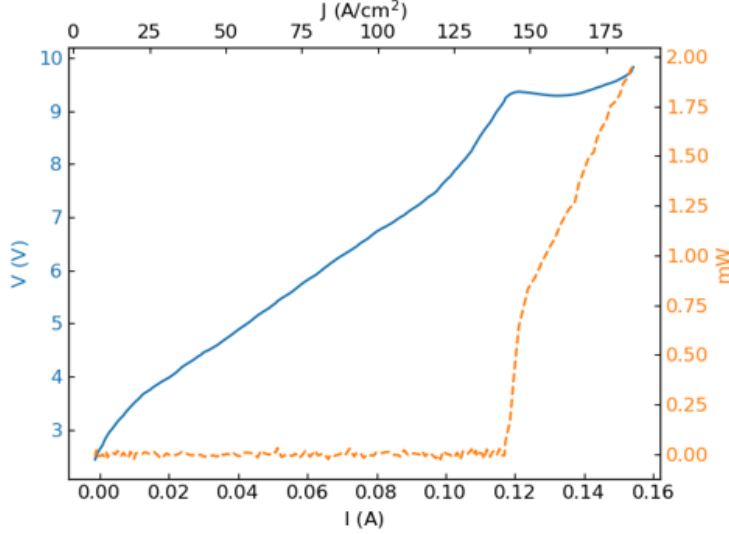


Figure 21: LIV for laser 1, with threshold at 120mA with NDR at 160mA.

The threshold can be identified to be at 120mA, while the NDR seems to start around 160mA. Next, the LIV of "laser 2" is shown in figure (22).

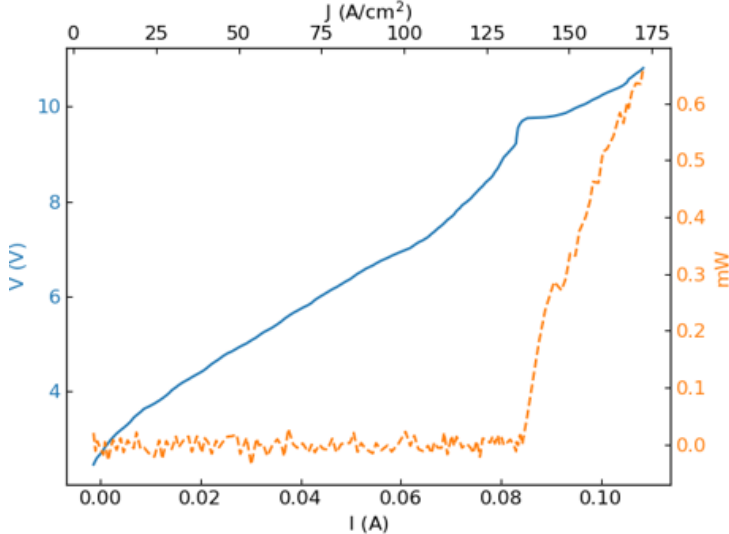


Figure 22: LIV for laser 2, with threshold at 83mA with NDR above 110mA.

The threshold can be identified at 83mA, with the NDR not being in the range of the experiment, e.g. it is expected to be at a current higher than 110mA. Additionally, the device contains a single-mode injector, but as figure (23) shows, it never lased.

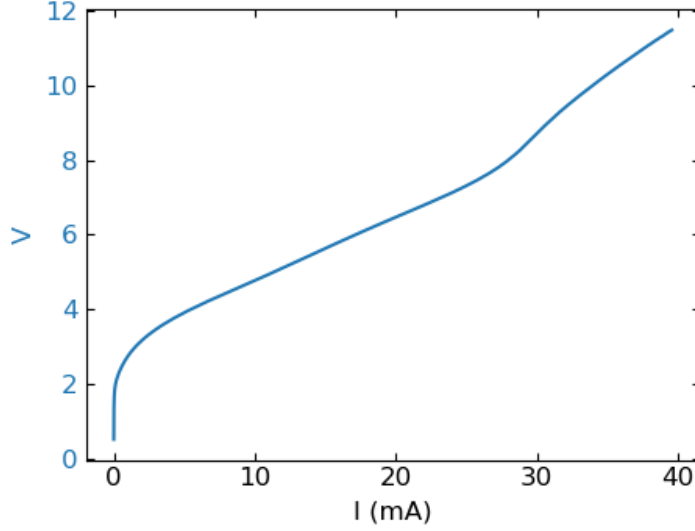


Figure 23: The IV curve of the non-lasing injector.

Further, we see a big slope efficiency of $\frac{dP}{dI} = 123 \text{ mW/A}$ for laser 1 in figure (24).

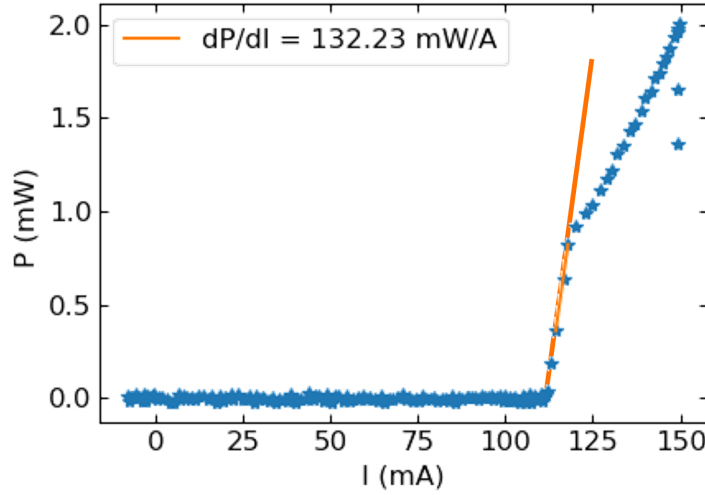


Figure 24: The slope efficiency dP/dI plotted as a function of the current.

Figure (24) shows a much bigger slope efficiency than for standard cleaved devices, which goes hand in hand with a large jump in differential resistances at the threshold, as figure (25) and (26) show. Due to the tapering, indeed, the mirror reflectivity is very low.

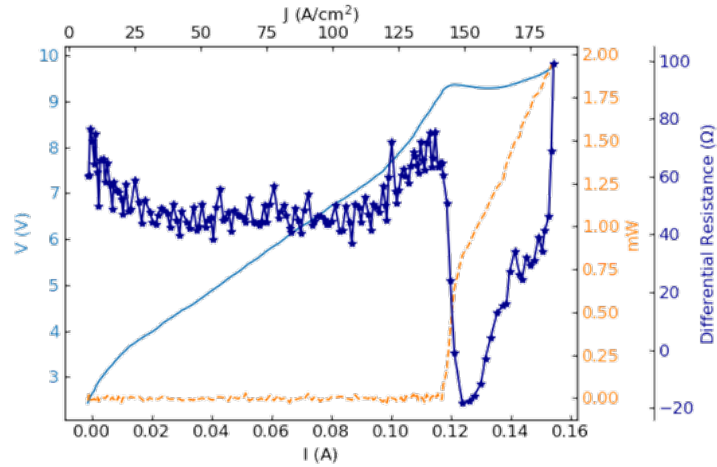


Figure 25: The differential resistance plotted vs the current, for laser 1.

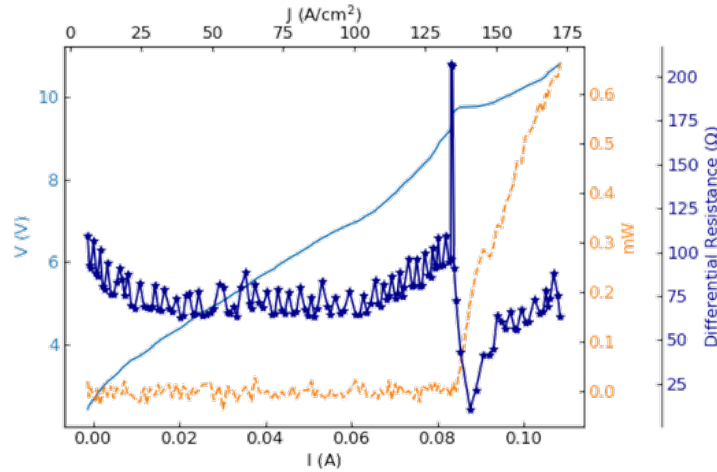


Figure 26: The differential resistance plotted vs the current, for laser 2.

Since the sensitivity of a laser used as a detector depends on the ratio between the resistance below and above the threshold, these devices show good performances as detectors [8]. In figure (27), we see that the injector has only a minor influence on the performance of the laser. Namely, it only slightly increases the slope efficiency.

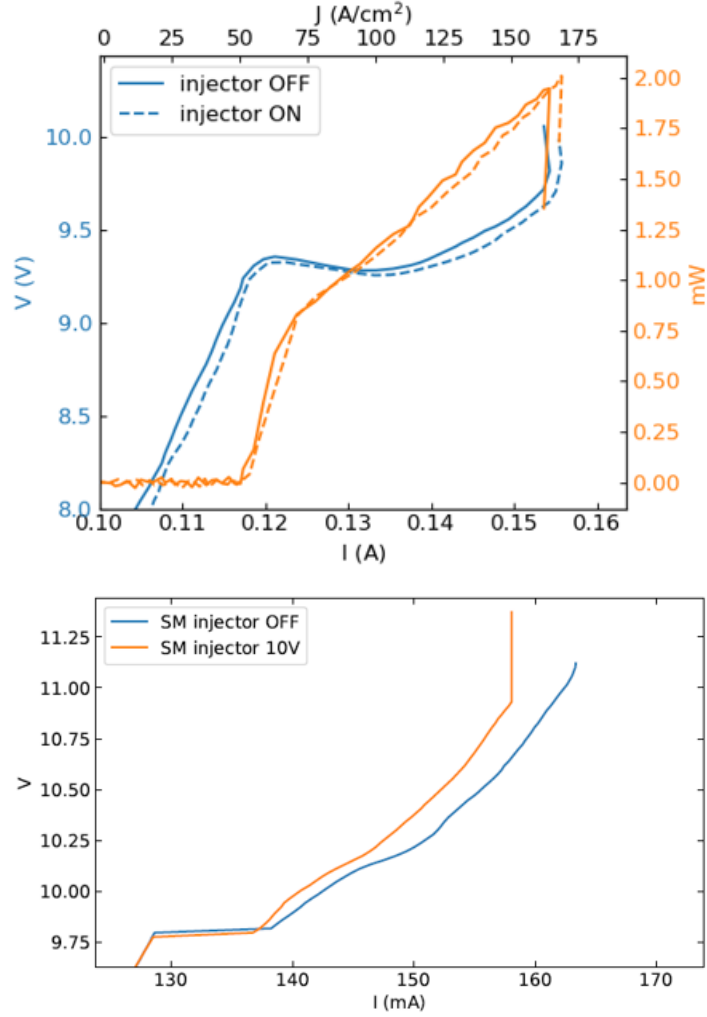


Figure 27: The effect of the injector on the LIV curve is small.

However, we observe yet another hysteretical behaviour around the threshold. Figures (28) and (29) show that the laser behaves differently if the current is ramped up vs when it is ramped down.

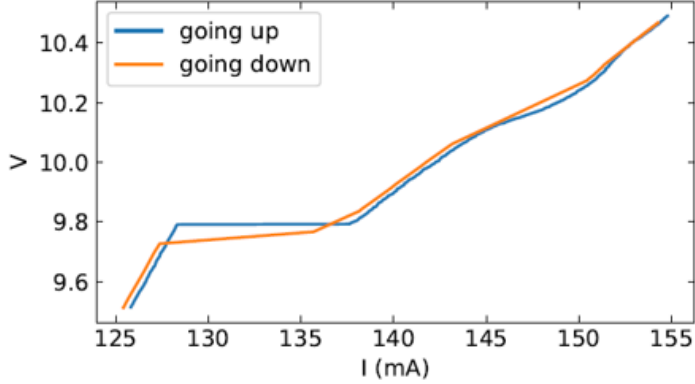


Figure 28: Hysteresis in the IV curve of laser 1.

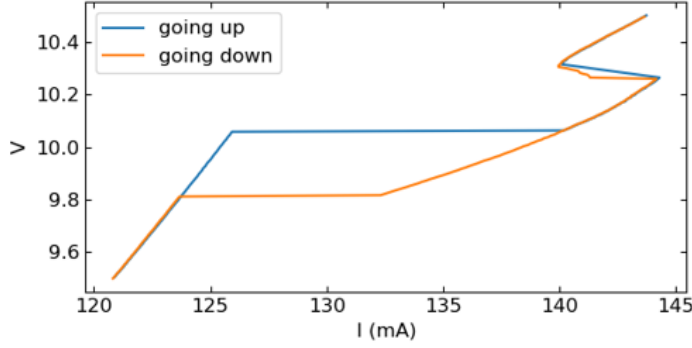


Figure 29: Hysteresis in the IV curve of laser 2.

Next, we will look at the spectra of the two lasers. Figure (30) shows the spectrum of laser 1 at 10.6V and 35dBm of injected RF at frequency 18.4GHz.

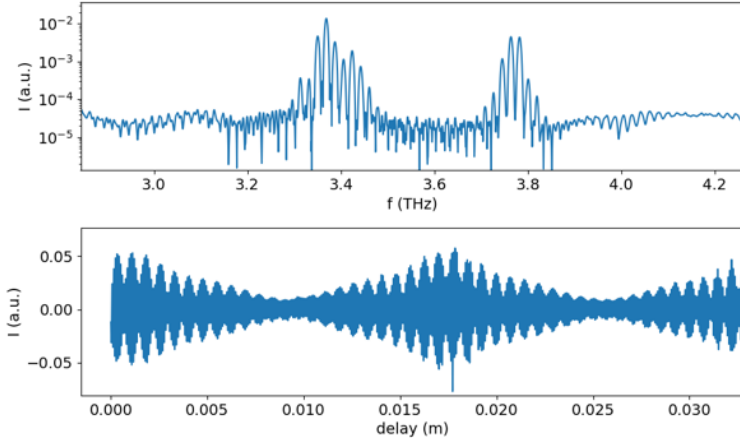


Figure 30: The spectrum of laser 1 at 10.6V and 35dBm of injected RF power and RF frequency 18.4GHz.

Figure (30) shows the spectrum of laser 2 at 10.6V and 35dBm of injected RF at

frequency 18.2GHz.

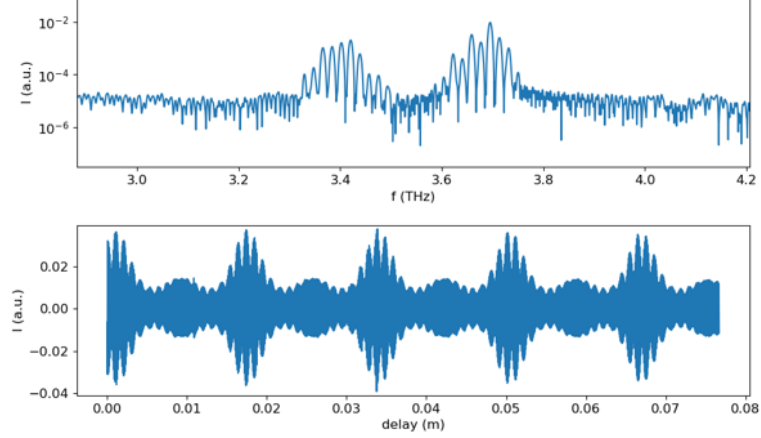


Figure 31: The spectrum of laser 2 at 10.6V and 35dBm of injected RF power and RF frequency 18.2GHz.

If both lasers run simultaneously, the spectrum changes as figure (32) shows.

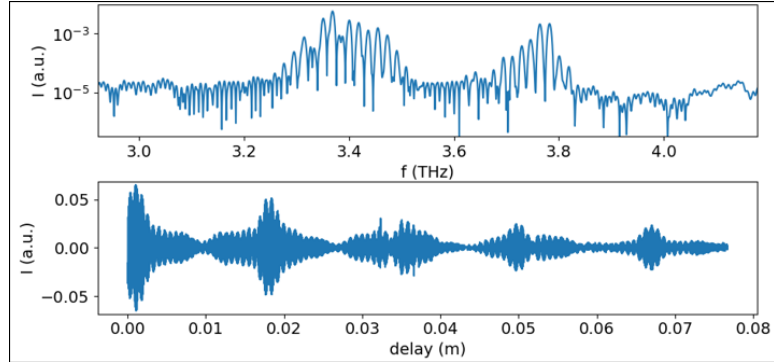


Figure 32: The spectrum when both lasers are turned on.

The interferogram is no longer symmetric since the two lasers are not fully locked. To see the effect of the injector on the dual comb, we measure heterodyne beatings of the two lasers, sweeping the voltage of one of the two from 10.758V to 10.64V with the injector on and off. Figure (33) shows the result.

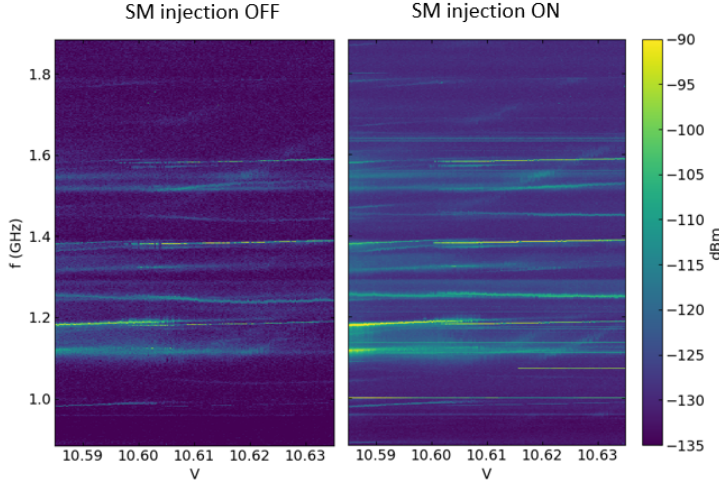


Figure 33: Comparison of the colour plot of the beat note at different voltages with injector on and off.

We can see that the injector brings no clear advantage. Thus, we zoom in on a maximum around 1.38GHz, and figure (34) shows that the linewidth is slightly reduced.

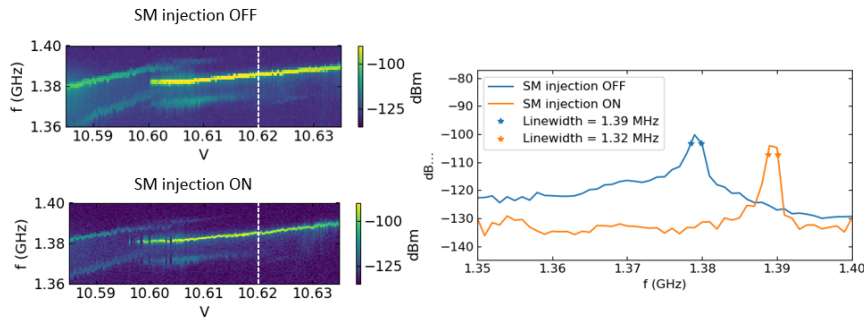


Figure 34: The effect of the injector on the beat note at $\approx 1.38\text{GHz}$ and linewidth at 10.62V.

We also zoom in on the maximum around 1.58GHz and see an improvement of the linewidth from 0.84MHz to 0.45MHz. This is shown in figure (35).

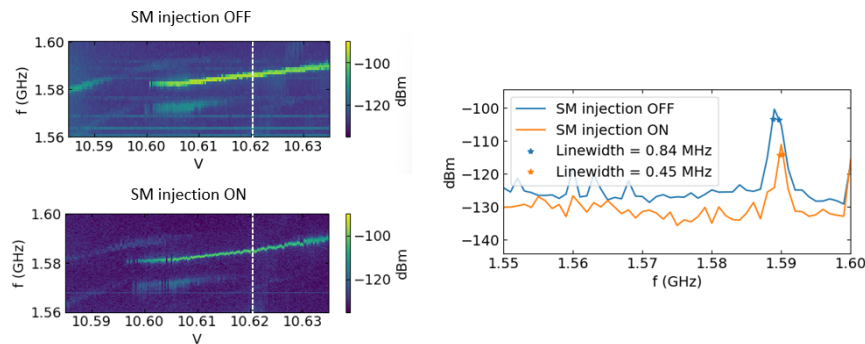


Figure 35: The effect of the injector on the beatnote at $\approx 1.58\text{GHz}$ and linewidth at 10.62V.

4 Discussion

A ring QCL with a bullseye antenna and a double ridge laser with a single-mode injector were investigated. The ring QCL showed hysteretic behaviour, which can be explained by considering that the ring QCL could have two main longitudinal supermodes with slightly different frequencies and effective refractive indices. This implies that their repetition frequencies $f_{\text{rep}}(n_{\text{eff}}) = c/(2Ln_{\text{eff}})$ will differ. Forcing the laser to move from a repetition frequency close to $f_{\text{rep}}(n_1)$ to one close to $f_{\text{rep}}(n_2)$ would induce the laser to move from mode 1 to mode 2.

The double ridge QCL also showed interesting results, though the single mode injector did not lase. Its influence on the QCL was small, but we were able to reveal its effect, especially on the linewidth of the heterodyne beat note. Due to their large slope efficiencies, the devices will be a good choice for a sensitive THz detector. The double ridge QCL also exhibited hysterical behaviour, which needs further study.

References

- [1] Quantum cascade lasers, explained by RP; minibands, QCL, mid-infrared, terahertz, semiconductor lasers.
- [2] Jérôme Faist. *Quantum Cascade Lasers*. Oxford University Press, 03 2013.
- [3] Ursula Keller. *Ultrafast Lasers: A Comprehensive Introduction to Fundamental Principles with Practical Applications*. Springer, 2022.
- [4] Bo Meng, Matthew Singleton, Johannes Hillbrand, Martin Francké, Mattias Beck, and Jérôme Faist. Dissipative kerr solitons in semiconductor ring lasers. 16(2):142–147. Number: 2 Publisher: Nature Publishing Group.
- [5] Dr Rüdiger Paschotta. Four-wave mixing.
- [6] Urban Senica, Andres Forrer, Tudor Olariu, Paolo Micheletti, Sara Cibella, Guido Torrioli, Mattias Beck, Jérôme Faist, and Giacomo Scalari. Planarized THz quantum cascade lasers for broadband coherent photonics. 11(1):347. Number: 1 Publisher: Nature Publishing Group.
- [7] Paolo Micheletti, Urban Senica, Andres Forrer, Sara Cibella, Guido Torrioli, Martin Franké, Mattias Beck, Jérôme Faist, and Giacomo Scalari. Terahertz optical solitons from dispersion-compensated antenna-coupled planarized ring quantum cascade lasers. 9(24):eadf9426. Publisher: American Association for the Advancement of Science.
- [8] Paolo Micheletti, Jérôme Faist, Tudor Olariu, Urban Senica, Mattias Beck, and Giacomo Scalari. Regenerative terahertz quantum detectors. *APL Photonics*, 6(10):106102, 10 2021.
- [9] David Burghoff. Some notes on shifted wave interference fourier transform spectroscopy (swifts). [Online], 2020. Accessed November 19, 2024.
- [10] Wikiwand - liquid helium.
- [11] The quantum cascade laser – quantum optoelectronics group | ETH zurich.
- [12] Dr Rüdiger Paschotta. Kerr effect.
- [13] Ian Coddington, Nathan Newbury, and William Swann. Dual-comb spectroscopy. 3(4):414–426. Publisher: Optica Publishing Group.
- [14] Ina Heckelmann, Mathieu Bertrand, Alexander Dikopoltsev, Mattias Beck, Giacomo Scalari, and Jérôme Faist. Quantum walk comb in a fast gain laser. 382(6669):434–438. Publisher: American Association for the Advancement of Science.
- [15] Francesco Cappelli, Luigi Consolino, Giulio Campo, Iacopo Galli, Davide Mazzotti, Annamaria Campa, Mario Siciliani de Cumis, Pablo Cancio Pastor, Roberto Eramo, Markus Rösch, Mattias Beck, Giacomo Scalari, Jérôme Faist, Paolo De Natale, and Saverio Bartalini. Retrieval of phase relation and emission profile of quantum cascade laser frequency combs. 13(8):562–568. Number: 8 Publisher: Nature Publishing Group.
- [16] Gustavo Villares, Andreas Hugi, Stéphane Blaser, and Jérôme Faist. Dual-comb spectroscopy based on quantum-cascade-laser frequency combs. 5(1):5192. Number: 1 Publisher: Nature Publishing Group.

- [17] Andreas Hugi, Gustavo Villares, Stéphane Blaser, H. C. Liu, and Jérôme Faist. Mid-infrared frequency comb based on a quantum cascade laser. 492(7428):229–233. Number: 7428 Publisher: Nature Publishing Group.
- [18] David Burghoff. Some notes on shifted wave interference fourier transform spectroscopy (swifts), 07 2018.